Identification and Characterization of Receptor-Specific Peptides for siRNA Delivery

Citation	Ren, Yin, Sabine Hauert, Justin H. Lo, and Sangeeta N. Bhatia. 2012. Identification and characterization of receptor-specific peptides for siRNA delivery. ACS Nano 6(10): 8620-8631.
Published Version	doi:10.1021/nn301975s
Accessed	February 19, 2015 11:50:53 AM EST
Citable Link	http://nrs.harvard.edu/urn-3:HUL.InstRepos:10511099
Terms of Use	This article was downloaded from Harvard University's DASH repository, and is made available under the terms and conditions applicable to Other Posted Material, as set forth at http://nrs.harvard.edu/urn-3:HUL.InstRepos:dash.current.terms-of-use#LAA

(Article begins on next page)

Identification and Characterization of Receptor-Specific Peptides for siRNA Delivery

Yin Ren,[†,‡] Sabine Hauert,[†] Justin H. Lo,[†] and Sangeeta N. Bhatia[†,§,⊥,¶,#,*]

[†]Harvard—MIT Division of Health Sciences and Technology, Massachusetts Institute of Technology, Cambridge, Massachusetts 02139, United States, [‡]Medical Scientist Training Program, Harvard Medical School, Boston, Massachusetts 02115, United States, [§]Broad Institute of Harvard and MIT, Cambridge, Massachusetts 02142, United States, [⊥]Department of Medicine, Brigham and Women's Hospital, Boston, Massachusetts 02115, United States, [¶]Electrical Engineering and Computer Science, David H. Koch Institute for Integrative Cancer Research, Massachusetts Institute of Technology, Cambridge, Massachusetts 02139, United States, and [#]Howard Hughes Medical Institute, Chevy Chase, Maryland 20815, United States

RNA interference (RNAi) offers an attractive means to silence gene expression with extraordinary specificity, particularly for the subset of candidate therapeutic gene targets that are considered "undruggable".[1] This capability is particularly appealing for diseases with complex genotypic alterations such as cancer. However, siRNA molecules are large (~14 kDa), highly anionic (~40 negative charges), hydrophilic, and susceptible to degradation by nucleases. Upon systemic administration, naked siRNAs cannot penetrate into tumor tissue, target extravascular cancer cells, or cross cellular membranes to act in the cytosol. Therefore, to bring RNA-based therapeutics into the clinic, one must improve the pharmacokinetic properties of siRNA and overcome several delivery barriers.[2,3]

Approaches to target the delivery of siRNA to tumor cells include lipophilic conjugations such as cholesterol,[4] attachment to targeting moieties such as antibodies or aptamers,[5,6] or encapsulation in polymer-based or liposomal carriers targeting tumor-specific markers.[7] Nonetheless, to date, none of these approaches enable active penetration into the tumor parenchyma to achieve gene silencing in epithelial tumor cells where genetic alterations reside. Elsewhere, cell penetrating peptides (CPP, also known as protein transduction domains) such as TAT and poly-arginine have been shown to bring DNA- and RNA-based payloads into the cytosol.[8] While CPPs represent a promising class of siRNA carriers that rapidly penetrates the cell membrane, they lack receptor specificity; they bind to and are internalized by cells *via* heparan sulfates and other glycosaminoglycans in nearly all cell types *in vitro* and *in vivo*.[9,10] Thus, an ideal siRNA

ABSTRACT
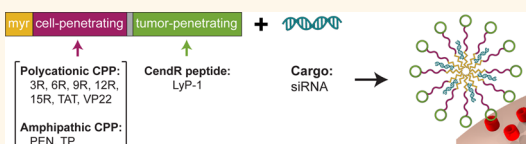
Tumor-targeted delivery of siRNA remains a major barrier in fully realizing the therapeutic potential of RNA interference. While cell-penetrating peptides (CPP) are promising siRNA carrier candidates, they are universal internalizers that lack cell-type specificity. Herein, we design and screen a library of tandem tumor-targeting and cell-penetrating peptides that condense siRNA into stable nanocomplexes for cell type-specific siRNA delivery. Through physiochemical and biological characterization, we identify a subset of the nanocomplex library of that are taken up by cells *via* endocytosis, trigger endosomal escape and unpacking of the carrier, and ultimately deliver siRNA to the cytosol in a receptor-specific fashion. To better understand the structure—activity relationships that govern receptor-specific siRNA delivery, we employ computational regression analysis and identify a set of key convergent structural properties, namely the valence of the targeting ligand and the charge of the peptide, that help transform ubiquitously internalizing cell-penetrating peptides into cell type-specific siRNA delivery systems.

KEYWORDS: siRNA delivery · tumor-penetrating peptides · cell-penetrating peptides · LyP-1 · cancer therapy

delivery system should possess two complementary characteristics: it should efficiently penetrate tissues and cross cellular membranes, but it should also be cell type-specific by targeting only tumor cells while sparing normal cells. Efforts to enhance the specificity of CPPs include attachment to homing peptides or restriction of cargo activity to specific cells.[11−13] However, the development of receptor-specific CPPs has been a highly empirical process: peptides were tested one at a time without systematic optimization of functional properties.

Consequently, tumor-specific delivery of siRNA by CPPs is not routinely achieved.

Recently, a new class of cell-internalizing and tumor-penetrating peptides has been described which leverage a consensus C-terminal (R/K)XX(R/K) motif (the CendR rule) to activate transvascular transport, cell internalization, and parenchyma penetration.[14,15] Two peptides that both contain tumor-homing and cryptic CendR motifs, iRGD (CRGDKGPDC) and LyP-1 (CGNKRTRGC), have been shown to significantly improve the delivery of small molecules, antibodies, and nanoparticles to tumors.[16] Leveraging this discovery, we have previously developed tandem peptide sequences bearing a constant tumor-penetrating domain (LyP-1) and variable cell-penetrating/siRNA-binding domains to chaperone siRNA cargo deep into the parenchyma of ovarian tumors in vivo and suppress a novel ovarian oncogene.[17] However, the intracellular trafficking mechanism by which siRNAs are delivered to tumor cells expressing specific receptors remains incompletely understood. Furthermore, the structure–activity relationships that favor cell internalization and maximize gene silencing, while maintaining cell type-specific penetration have yet to be determined.

Here, we present a more in-depth analysis of cell penetrating peptides to better understand the properties that govern receptor-specific siRNA delivery. We characterized a library of tumor-penetrating nanocomplexes formed by siRNAs noncovalently bound to tumor-specific peptides bearing structurally distinct cell-penetrating domains. A subset of nanocomplexes achieved functional delivery of siRNA in a cell type-specific manner. To gain quantitative mechanistic insights, we studied the intracellular trafficking mechanisms by measuring siRNA uptake, escape from endosomal entrapment, and dissociation of siRNA from the carrier. To understand the relationship between peptide structural properties and receptor-specific siRNA delivery, we fused data from physiochemical characterizations with regression modeling to derive structure–activity relationships. Two properties, the valence of the tumor-specific ligand on the nanocomplex and peptide charge, are key considerations when designing a siRNA delivery system to knock down genes in a receptor-specific manner. Specifically, we found that myr-TP-LyP-1 met the desired material properties, condensed siRNA into nanocomplexes that are multivalent, and delivered siRNA to human cancer cell lines in a receptor-specific fashion.

RESULTS AND DISCUSSION

Design and Characterization of Tandem Peptides. To develop tumor-specific and cell-penetrating peptides for siRNA delivery, we set the following design criteria: the delivery system should noncovalently condense siRNA in a single step, remain stable in physiologic conditions, multivalently display homing peptides for tumor-targeting, and readily dissociate once inside the cytosol to enable siRNA incorporation into the

RNA-induced silencing complex (RISC). Toward this goal, we synthesized a library of 9 tandem peptide carriers composed of distinct cell penetrating domains at the NH_2-terminus and a tumor-targeting/penetrating CendR peptide, LyP-1 (CGNKRTRGC), at the C-terminus (Figure 1A and Table 1). LyP-1 homes to tumor cells and tumor lymphatics via binding to its receptor p32, a mitochondrial protein that is aberrantly expressed on the surface of tumor cells and tumor-associated macrophages.[18,19] We generated N-terminally myristoylated versions of each of the nine tandem peptides, since myristoylation has been shown to enhance hydrophobic interactions and peptide affinity to lipid bilayers such as the cell membrane.[20] The selection of cell-penetrating domains included representatives of polycationic sequences including oligoarginines, the HIV TAT protein,[21] and the HSV-1 tegument protein VP22;[22] as well as amphipathic CPPs such as penetratin[23] and Transportan.[24] To reduce the risk that siRNA complexation interfered with receptor targeting, the cell-penetrating and tumor-targeting domains were separated by a four-glycine spacer.

We found that tandem peptides readily condensed siRNA into tumor-penetrating nanocomplexes (TPN) in a one-step procedure (Figure 1B). To determine the amount of peptide needed to fully encapsulate free siRNAs into stable nanocomplexes, we mixed siRNA with each tandem peptide at increasing molar ratios in the presence of a dye (TO-PRO-3) that fluoresces when intercalated into double-stranded nucleic acids. Upon particle formation, we observed a decrease in dye fluorescence likely due to steric exclusion of dye binding to siRNA by peptides in the nanocomplex (Figure 1B). Near-maximal (>95%) encapsulation of siRNA occurred consistently at molar ratios between 1.6:1 and 20:1 (peptide-to-siRNA) for all peptides in the library. Since the positively charged CPP domain binds the negatively charged backbone of the siRNA, a higher encapsulation ratio would result in increased number of tandem peptides per each siRNA molecule, which in turn leads to a higher valence of LyP-1 in the nanocomplex.

Using TEM and dynamic light scattering (DLS), we observed that the majority of nanocomplexes have hydrodynamic diameters ranging from 50 to 100 nm in water and from 200 to 400 nm in PBS, with a narrow size distribution (polydispersity index < 0.2) (Figure 1C, D). The zeta potential ranges from +20 to +40 mV (Table 1). No significant change in size was observed when placed in mouse serum at 37 °C (Supporting Information, Figure S1A). Moreover, nanocomplexes remained intact for at least 24 h in phosphate-buffered saline (pH 7.1) at 37 °C as indicated by minimal change in TO-PRO-3 fluorescence (Figure 1E). To ensure that TO-PRO-3 fluorescence indeed corresponded to the presence of intact nanocomplexes, we disrupted nanocomplexes with a detergent and observed restoration
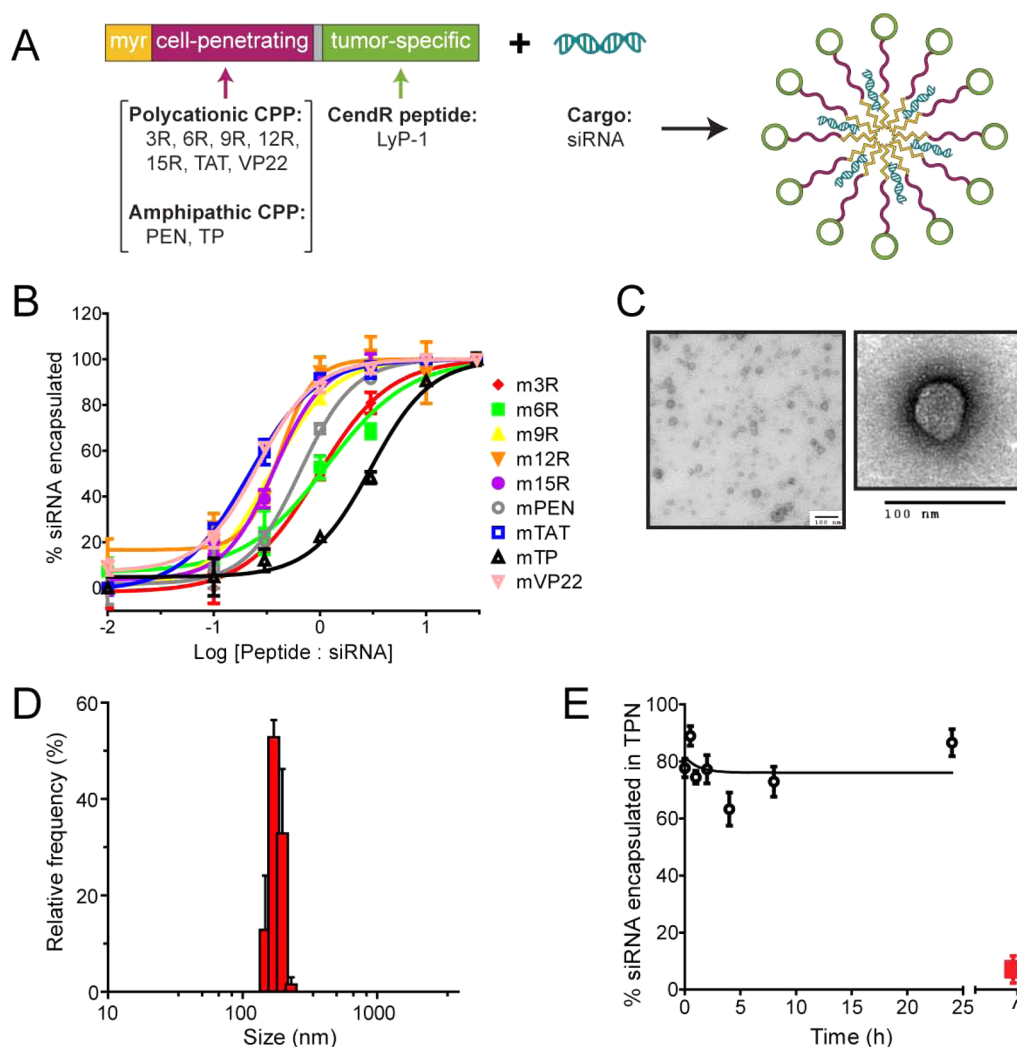
Figure 1. Design and characterization of tandem peptides. (A) Schematic representation of the tumor penetrating nanocomplex, with siRNA (blue) noncovalently bound to tandem peptides composed of a cyclic tumor-penetrating domain (LyP-1, green) and various cell-penetrating peptide domains (purple) separated by a 4-glycine spacer (gray). A subset of the tandem peptides tested were *N*-myristoylated (myr, orange). Cell-penetrating peptide domains tested include representatives from both polycationic and amphipathic CPPs. **(B)** Encapsulation of siRNA by tandem peptides. Tandem peptides were mixed with siRNA at varying molar ratios, and the amount of siRNA encapsulated in nanocomplexes was determined by measuring the fluorescence of a nucleic-acid intercalating dye (TO-PRO-3) normalized to dye fluorescence with siRNA alone. **(C)** Representative TEM of a tandem peptide/siRNA nanocomplex formed in water and negatively stained with uranyl acetate; scale bar = 100 nm. **(D)** Hydrodynamic size histograms of nanocomplexes in phosphate-buffered saline (PBS) from dynamic light scattering measurements. **(E)** Stability of nanocomplexes in saline at 37 °C, as measured by intercalation of TO-PRO-3 dye. The final data point (red, marked with a circumflex (∧)) represents disruption with 0.1% Triton-X 100 detergent. Error bars indicate standard deviation (SD) from three independent experiments.

of dye fluorescence (Figure 1E). These results collectively suggest that tandem peptides can noncovalently condense siRNA into stable nanocomplexes at defined molar ratios.

Cellular Uptake of Nanocomplexes. To effectively deliver siRNA, the carrier should exhibit high cellular uptake with minimal cytotoxicity. We examined a panel of established, human cancer cell lines and identified three (HeLa, MDA-MB-435, and OVCAR-8) that overexpress p32, the cognate receptor for the tumor-penetrating domain, LyP-1, on the cell surface. Viability of HeLa cells was not affected for the majority of tandem peptides with the exception of 12R and 15R,

whose excess cationic charges may have contributed to disruption of membrane integrity and reduction in cell viability (Supporting Information, Figure S1B, S1C). To gain insight into the siRNA delivery capabilities, we used flow cytometry to assess the effect of NH_2-terminal myristoylation of the carrier on the cellular uptake of siRNA. In OVCAR-8 human ovarian cancer cells, the myristoylated species of the tandem peptides were significantly more efficacious in delivering fluorescently labeled siRNA relative to their nonmyristoylated counterparts (Figure 2A). This change may be due to enhanced particle stability due to hydrophobic interactions between myristoyl moieties, or enhanced

TABLE 1. Structural Properties of Peptide/siRNA Nanocomplexes

name	sequence[a]	diameter (nm)[b]	ζ-potential (mV)[c]
3R	(dR)$_3$GGGGK(TAMRA)CGNKRTRGC	517.0 ± 33.9	7.8 ± 5.6
6R	(dR)$_6$GGGGK(TAMRA)CGNKRTRGC	364.3 ± 42.0	11.6 ± 8.6
9R	(dR)$_9$GGGGK(TAMRA)CGNKRTRGC	291.7 ± 21.2	ND
12R	(dR)$_{12}$GGGGK(TAMRA)CGNKRTRGC	175.5 ± 42.3	ND
15R	(dR)$_{15}$GGGGK(TAMRA)CGNKRTRGC	211.4 ± 18.9	ND
PEN	RQIKIWFQNRRMKWKKGGGGK(TAMRA)CGNKRTRGC	259.0 ± 36.1	ND
TAT	GRKKRRQRRRGYKGGGGK(TAMRA)CGNKRTRGC	175.3 ± 5.5	ND
TP	GWTLNSAGYLLGKINLKALAALAKKILGGGGK(TAMRA)CGNKRTRGC	310.5 ± 61.2	ND
VP22	DAATATRGRSAASRPTERPRAPARSASRPRRPVDGGGGK(TAMRA)CGNKRTRGC	253.5 ± 6.5	ND
m3R	myr-(dR)$_3$GGGGK(TAMRA)CGNKRTRGC	209.0 ± 40.5	21.8 ± 5.0
m6R	myr-(dR)$_6$GGGGK(TAMRA)CGNKRTRGC	151.0 ± 11.1	27.3 ± 4.0
m9R	myr-(dR)$_9$GGGGK(TAMRA)CGNKRTRGC	207.8 ± 19.6	36.6 ± 7.1
m12R	myr-(dR)$_{12}$GGGGK(TAMRA)CGNKRTRGC	191.2 ± 17.9	27.6 ± 15.0
m15R	myr-(dR)$_{15}$GGGGK(TAMRA)CGNKRTRGC	377.2 ± 49.4	36.0 ± 7.5
mPEN	myr-RQIKIWFQNRRMKWKKGGGGK(TAMRA)CGNKRTRGC	337.6 ± 54.9	29.0 ± 5.1
mTAT	myr-GRKKRRQRRRGYKGGGGK(TAMRA)CGNKRTRGC	194.6 ± 43.6	35.8 ± 8.0
mTP	myr-GWTLNSAGYLLGKINLKALAALAKKILGGGGK(TAMRA)CGNKRTRGC	343.6 ± 32.3	31.9 ± 3.7
mVP22	myr-DAATATRGRSAASRPTERPRAPARSASRPRRPVDGGGGK(TAMRA)CGNKRTRGC	233.0 ± 58.8	30.8 ± 4.8

[a] The myr- prefix denotes NH$_2$-terminal myristoylation. Peptide abbreviations are as follows: (dR)$_n$ = oligoarginine where n is the number of D-arginine residues; PEN = penetratin; TAT = HIV TAT (48−60); TP = transportan; VP22 = HSV-1 VP22 protein. [b] Mean hydrodynamic size based on dynamic light scattering measurements. Errors indicate SD from at least three separate measurements. [c] Zeta-potential of nanocomplexes. Errors indicate SD from at least three independent measurements. ND, not determined.

interactions between myristoylated peptides and membrane lipids. To confirm that siRNA delivery was indeed correlated with uptake of the carrier, we repeated the experiments with tandem peptides singly labeled with tetramethylrhodamine (TAMRA) and compared intracellular peptide fluorescence with siRNA fluorescence for each peptide (Figure 2B). In general, the relative cellular uptake of the carrier correlated linearly with that of the siRNA cargo. Short oligo-arginine CPPs such as 3R and 6R achieved poor siRNA delivery in comparison to longer poly-arginines such as 12R and 15R, likely due to the lower number of cationic charges available to bind the negatively charged siRNA backbone and provide sufficient charge shielding for membrane translocation. Similar patterns in cellular uptake were observed in MDA-MB-435 and HeLa cells (not shown). Collectively, these results indicate that a subset of tandem peptides can effectively carry siRNA payloads into cell lines that express p32 on the surface; additionally, N-terminal myristoylation of the peptide carrier can further enhance siRNA delivery into the cell, likely by improving peptide lipophillicity and cellular uptake.

Next, we assessed whether siRNA delivery by nanocomplexes is cell type-specific. To confirm p32 receptor-specificity, we utilized flow cytometry to examine siRNA uptake in the presence of a monoclonal antibody (mAb 60.11) directed against the NH$_2$-terminus of p32 polypeptide.[18] In OVCAR-8 cells, uptake of nanocomplexes bearing CPP domains such as TAT, 9R, 12R, and 15R was unaltered in the presence of the antibody. In contrast, the p32 antibody reduced siRNA delivery by TP, 3R, 6R, and PEN nanocomplexes in a dose-dependent manner by up to 80% (Figure 2C,D). Compared to cationic CPPs such as 12R and 15R that formed nanocomplexes at a peptide-to-siRNA molar ratio of nearly 1:1, TP-, 3R-, and 6R-LyP-1 nanocomplexes were formed at a ratio of at least 9:1, resulting in a larger number of peptides per each siRNA molecule, and thus a higher LyP-1 valence in the nanocomplex. Since multivalent receptor−ligand interactions enhance specificity through avidity effects,[25,26] the higher p32-affinity (lower IC$_{50}$ of mAb) observed for this subset of nanocomplexes (TP, 3R, 6R) is attributable to multivalency effects.

Gene Silencing with Nanocomplexes. We next set out to determine the *in vitro* gene silencing activity of siRNAs delivered by nanocomplexes. HeLa cells stably expressing a destabilized green fluorescence protein reporter (dGFP) were used as a model system for direct quantification of the RNAi response. Cells were treated with siRNA against GFP bound to either tandem peptides or lipofectamine and analyzed by flow cytometry for GFP knockdown. Consistent with previous findings that myristoylation improves cellular uptake, myrisoylated carriers were more efficient in delivering siRNA and suppressing GFP expression than nonmyristoylated ones (Figure 3A,B and Supporting Information, Figure S2A). Six of nine tandem peptide carriers were able to silence GFP expression by over 50%, as determined by comparing the geometric means of the entire cell population. The degree of GFP suppression correlated with the dose of siRNA (Supporting Information, Figure S2B), was detectable starting at 24 h, and was maintained through at least 48 h after transfection (Figure S2C).

For tumor-specific siRNA delivery, an ideal system should target the delivery of siRNA to tumor cells while sparing nontumor or essential cells. To quantitatively
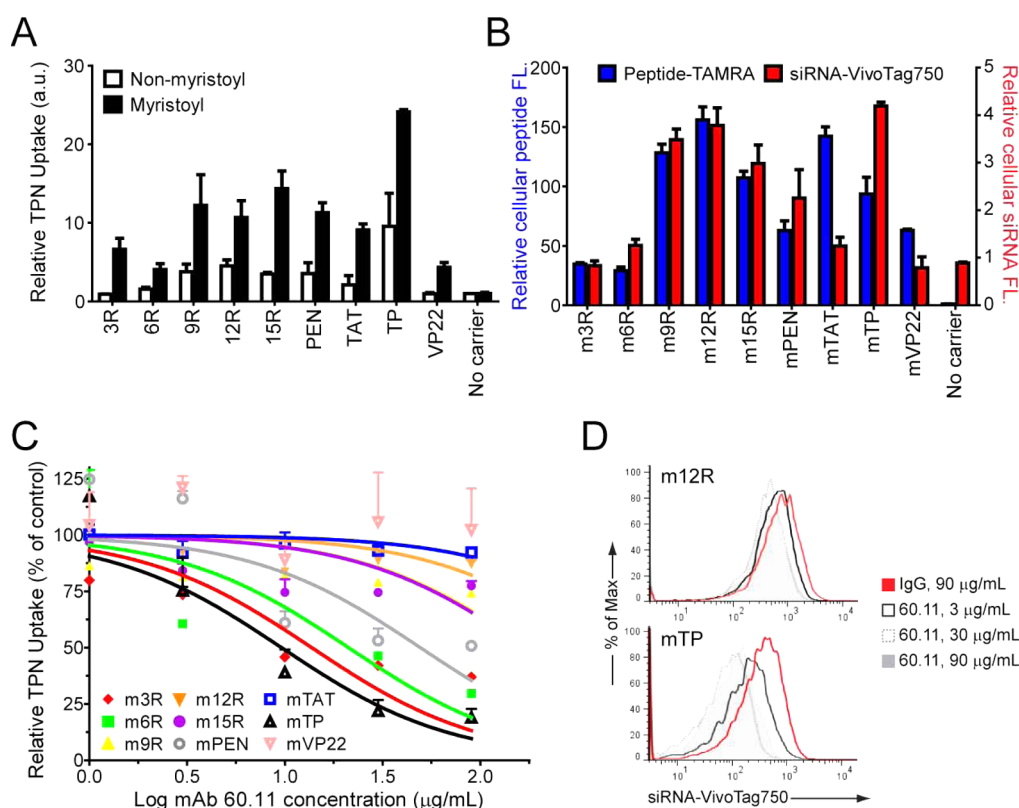
Figure 2. Cellular uptake of nanocomplexes. (A) OVCAR-8 ovarian cancer cells were incubated with nanocomplexes carrying siRNA labeled with a near-infrared fluorophore (VivoTag-S750). Cellular uptake is assessed by flow cytometry for both nonmyristoylated and myristoylated tandem peptides. Error bars indicate SD from 4 to 6 independent experiments. (B) Cellular uptake of TAMRA-labeled peptides (blue) with VivoTag-S750-labeled siRNA (red) in OVCAR-8 cells. Error bars indicate SD from 4 to 6 independent experiments. (C) Uptake by OVCAR-8 cells in the presence of increasing concentrations of a p32-specific monoclonal antibody (mAb 60.11). Uptake of nanocomplexes was normalized to that without antibody inhibition. Error bars indicate SD from 6 independent experiments. (D) Representative histograms from flow cytometry for cellular uptake of myr-12R-LyP-1 (top, m12R) and myr-TP-LyP-1 (bottom, mTP), in the presence of indicated concentrations of mAb 60.11 (black and gray) or a IgG control (red).

assess the ability of nanocomplexes to deliver siRNA in a receptor-specific fashion, we measured the "fitness" of each candidate nanocomplex as the normalized sum of gene silencing efficiency and p32-receptor specificity (normalized $1/IC_{50}$ of mAb 60.11) (Figure 3C,D). In particular, VP22 exhibits low fitness because cellular uptake was non-cell-type specific and gene knockdown was also poor. By contrast, nanocomplexes bearing polycationic CPP domains (12R and 15R) readily penetrated cellular membranes and carried siRNA into the cytosol; however, they do so in a non-cell-type specific manner as the presence of excess cationic charges likely abrogated receptor-specificity, resulting in low fitness. In comparison, cellular uptake by amphipathic CPPs such as PEN and TP is blocked by a p32-specific antibody, suggesting that the receptor-specificity of the LyP-1 domain is retained; nevertheless, TP nanocomplexes are much more efficient than PEN in suppressing gene expression. Indeed, the nanocomplex formed with myr-TP-LyP-1 has the highest fitness value of all carriers, owing to both potency in knockdown (>50% suppression of GFP) and p32 receptor specificity (lowest IC_{50} of mAb 60.11).

Intracellular Trafficking of Nanocomplexes. Our results thus far have demonstrated that for a given tumor-specific ligand, the tandem presentation of various universally internalizing CPP domains can lead to varying degrees of fitness. A subset of nanocomplexes was found to be taken up in a p32 receptor-specific fashion, and subsequently delivered siRNA to achieve efficient gene knockdown. To better understand the molecular properties that favored the conversion of a ubiquitously internalizing peptide into a receptor-specific siRNA delivery system, we next investigated the intracellular trafficking mechanisms by which nanocomplexes carry siRNA payloads into the cytosol.

We applied myr-TP-LyP-1 nanocomplexes carrying siRNAs labeled with a near-infrared fluorophore to HeLa cells and visualized intracellular trafficking via fluorescence microscopy. Fluorescent siRNAs were present in punctate vesicular structures consistent with sequestration in endosomes (Figure 4A). To directly confirm the intracellular localization of siRNAs, nanocomplexes were applied to HeLa cells either expressing a marker of early endosomes (Rab5a) or prelabeled with a pH-sensitive marker of endolysosomes
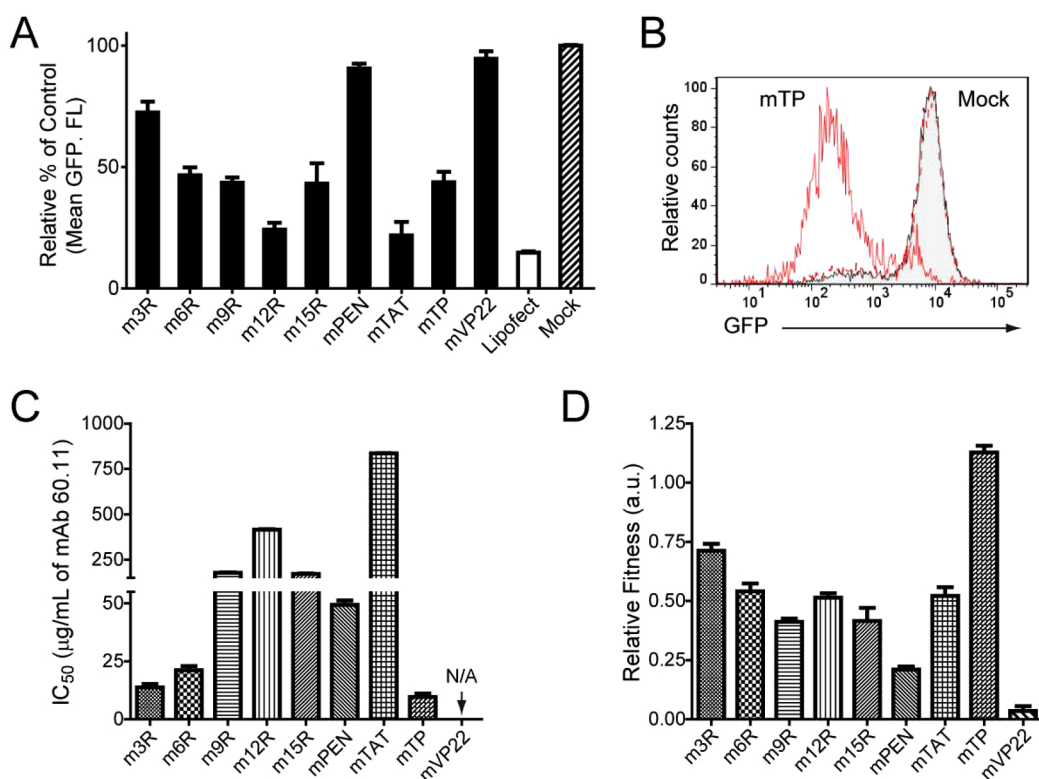
Figure 3. Nanocomplex-mediated receptor-specific gene silencing *in vitro*. (A) HeLa cells stably expressing destabilized GFP were transfected with nanocomplexes carrying siRNA against GFP. The amount of GFP knockdown was determined by flow cytometry 24 h later. Lipofectamine was used as a positive control. Error bars represent SD from cumulative data of three independent experiments. **(B)** Representative histograms for myr-TP-LyP1 nanocomplexes carrying *GFP*-specific siRNA. Mock treated cells are shaded in gray. **(C)** Receptor-specificity quantified as the concentration of p32-specific antibody to inhibit nanocomplex uptake by at least 50% (IC_{50}). Increasing concentrations of antibodies were added to cells for 1 h and subsequently in the presence of nanocomplexes for 4 h. Percent inhibition of nanocomplex uptake was determined by flow cytometry. IC_{50} values were derived by fitting a standard normalized dose−response curve for inhibitory binding effects. **(D)** The fitness of each nanocomplex, as determined by the normalized sum of knockdown efficiency and p32-specificity.

(Lysotracker). Fluorescently labeled siRNAs showed colocalization with both markers, suggesting that nanocomplexes carried siRNA payloads into the cell *via* endocytosis and were initially sequestered in endosomes.

We next sought to directly evaluate the ability of nanocomplexes to disrupt the endosomal membrane of HeLa cells and trigger the cytosolic release of cargo by codelivery with Calcein, a membrane-impermeable fluorophore.[27] In the presence of Calcein alone or with LyP-1 peptide lacking the CPP domain, a vesicular distribution indicative of little or no endosomal escape was observed (Figure 4B,C). By contrast, diffuse Calcein staining in up to 30% of cells suggestive of endosomal escape was seen with 12R, 15R, and TP tandem peptides (Figure 4B). Endosomal escape was carrier dose-dependent (Supporting Information, Figure S3A) and was partially dependent on the proton sponge effect,[28] as the escape efficiency correlated linearly with the number of arginines. In addition, *N*-myristoylated peptides were generally more efficient in enabling Calcein entry into the cytosol than their nonmyristoylated counterparts, consistent with enhanced interactions between myristic acid and membrane lipids on the

endosome that likely generate transient pores to allow leakage of molecules.[29] A similar pattern of endosomal escape results was observed when OVCAR-8 cells were examined (Supporting Information, Figure S3B).

To identify the trafficking pathways utilized by nanocomplexes after endocytosis, we examined the cellular uptake of myr-TP-LyP-1 nanocomplexes in the presence of small molecule inhibitors that each blocks a component of the endocytosis pathway.[30] Nanocomplex uptake was significantly decreased when treated with amiloride, an inhibitor of macropinocytosis, PDMP, an inhibitor of lipid-raft mediated endocytosis, and deoxyglucose, an inhibitor of ATP biosynthesis (Supporting Information, Figure S3C). In contrast, inhibitors of actin polymerization, clathrin-mediated endocytosis, or caveolae-mediated endocytosis did not interfere with cellular uptake.

To achieve gene knockdown, the carrier must ultimately dissociate from the siRNA cargo after escaping from the endosome to allow the incorporation of siRNA into the RISC machinery. To ascertain whether the carrier dissociates and releases siRNA subsequent to endosomal escape, we measured the relative amount of siRNA that dissociated from the carrier upon exposure to endolysosomal pH (pH 4−6) *via* monitoring the
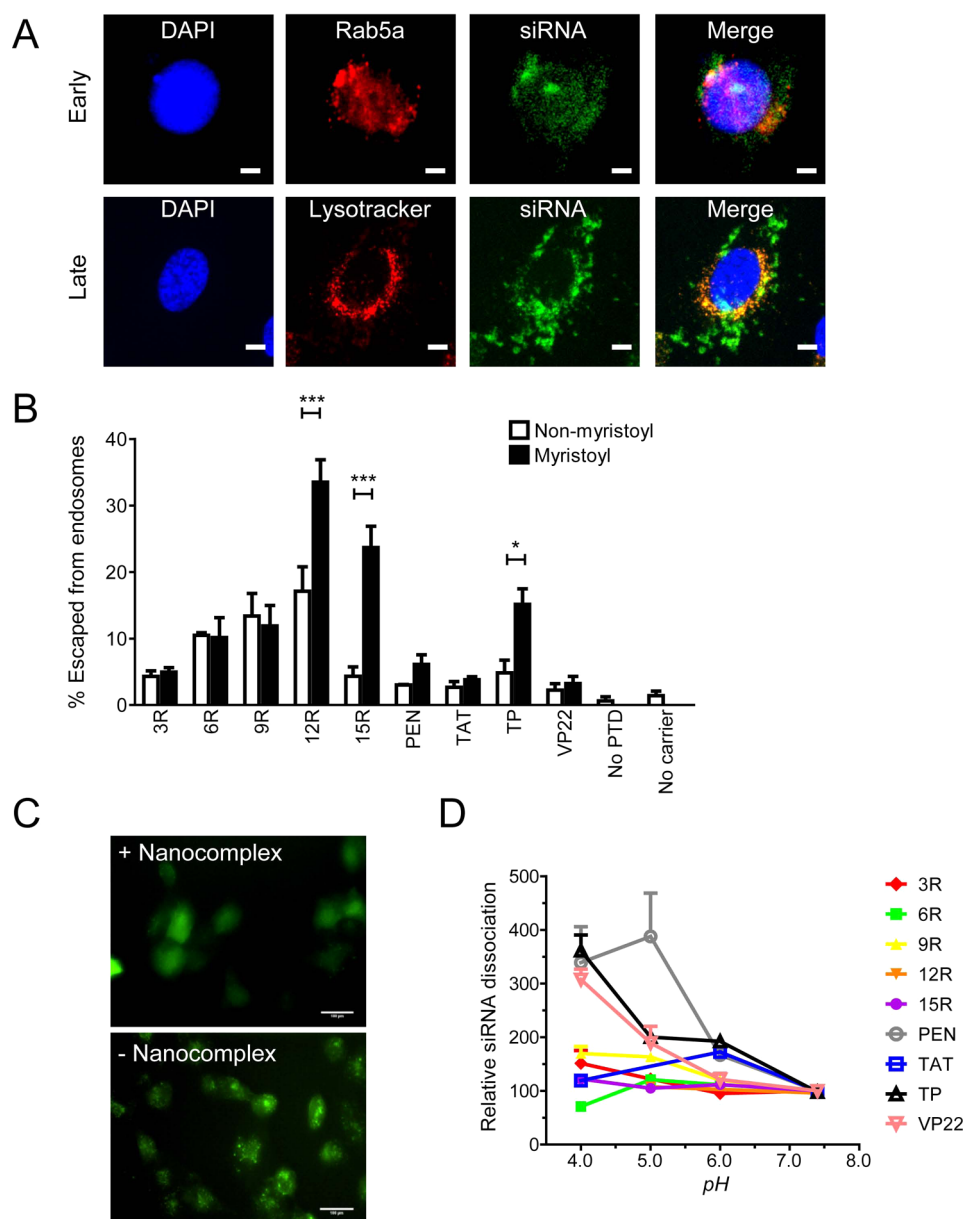
Figure 4. Intracellular trafficking mechanisms of nanocomplexes. (A, Top) Fluorescence microscopy images of human ovarian cancer cell line (OVCAR-8) transfected with Rab5a (CellLight Early Endosomes-GFP) 24 h prior (Early), and subsequently incubated with nanocomplexes carrying near-infrared fluorophore-labeled siRNA for 1 h. Images were pseudocolored for visualization: blue = DAPI; red = Rab5a; green = VivoTag-S750-siRNA. Co-localization of siRNA with the early endosomal marker is in yellow. Scale bar, 10 μm. **(A, Bottom)** Fluorescence microscopy images of HeLa cells after 4 h treatment with 100 nM FITC-siRNA encapsulated in myr-TP-LyP-1 nanocomplexes, in the presence of 50 nM Lysotracker dye to label late endosomes and endolysosomes (Late). Images are pseudocolored for visualization of colocalization: blue = DAPI; red = Lysotracker; green = FITC-siRNA. Scale bar, 10 μm. **(B)** Tandem peptide carriers enable the delivery of Calcein, a membrane impermeant dye, into the cytosol of HeLa cells. The mean percentage of cells displaying a uniform, cytosolic distribution of Calcein per each field of view was determined ($n = 500-800$ cells counted for each carrier). Error bars indicate SD from three independent experiments. ($*$) $p < 0.05$; ($***$) $p < 0.001$. **(C)** Representative fluorescence microscopy images of HeLa cells treated with nanocomplexes + Calcein (top) or Calcein alone (bottom) (green = Calcein). **(D)** Quantification of the relative amount of siRNA dissociated from the nanocomplex carriers at endolysosomal pH (pH = 4−6).

intercalation of TO-PRO-3 dye (Figure 4D). We observed that long poly-arginine peptides such as 12R and 15R did not readily release siRNA at low pH, likely due to the large number of positively charged arginines that retard the unpacking of siRNA. In comparison, amphipathic CPP species that are less cationic, such as PEN and TP, readily unpacked and dissociated

from siRNA at acidic pH. Taken together, these observations support a siRNA delivery mechanism that consisted of receptor-mediated endocytosis mediated by macropinocytosis and lipid-rafts, followed by escape from endosomal entrapment, and release of siRNA at acidic pH. Furthermore, factors such as peptide charge can affect the efficiency of nanocomplex unpacking,

TABLE 2. Parameters Used in the Computational Analysis[a]

concn (nM)	time (h)	diameter (nm)	diameter error (nm)	zeta (mV)	zeta error (mV)	LyP-1 valence	peptide charge	% K and/or R	charge density
100	24	209	40.5	21.8	5	11.03	6.6	41.18	0.39
100	24	151	11.1	27.3	4	31.16	9.6	50	0.48
100	24	207.8	19.6	36.6	7.1	2.732	12.6	56.52	0.55
100	24	191.2	17.9	27.6	15	1.186	15.6	61.54	0.6
100	24	377.2	49.4	36	7.5	1.912	18.6	65.52	0.64
100	24	337.6	54.9	29	5.1	5.604	10.6	36.67	0.35
100	24	194.6	43.6	35.8	8	1.843	12.6	48.15	0.47
100	24	343.6	32.3	31.9	3.7	35.68	7.6	19.51	0.19
100	24	233	58.8	30.8	4.8	1.457	9.6	27.08	0.2
100	48	209	40.5	21.8	5	11.03	6.6	41.18	0.39
100	48	151	11.1	27.3	4	31.16	9.6	50	0.48
100	48	207.8	19.6	36.6	7.1	2.732	12.6	56.52	0.55
100	48	191.2	17.9	27.6	15	1.186	15.6	61.54	0.6
100	48	377.2	49.4	36	7.5	1.912	18.6	65.52	0.64
100	48	337.6	54.9	29	5.1	5.604	10.6	36.67	0.35
100	48	194.6	43.6	35.8	8	1.843	12.6	48.15	0.47
100	48	343.6	32.3	31.9	3.7	35.68	7.6	19.51	0.19
100	48	233	58.8	30.8	4.8	1.457	9.6	27.08	0.2
50	24	209	40.5	21.8	5	11.03	6.6	41.18	0.39
50	24	151	11.1	27.3	4	31.16	9.6	50	0.48
50	24	207.8	19.6	36.6	7.1	2.732	12.6	56.52	0.55
50	24	191.2	17.9	27.6	15	1.186	15.6	61.54	0.6
50	24	377.2	49.4	36	7.5	1.912	18.6	65.52	0.64
50	24	337.6	54.9	29	5.1	5.604	10.6	36.67	0.35
50	24	194.6	43.6	35.8	8	1.843	12.6	48.15	0.47
50	24	343.6	32.3	31.9	3.7	35.68	7.6	19.51	0.19
50	24	233	58.8	30.8	4.8	1.457	9.6	27.08	0.2
50	48	209	40.5	21.8	5	11.03	6.6	41.18	0.39
50	48	151	11.1	27.3	4	31.16	9.6	50	0.48
50	48	207.8	19.6	36.6	7.1	2.732	12.6	56.52	0.55
50	48	191.2	17.9	27.6	15	1.186	15.6	61.54	0.6
50	48	377.2	49.4	36	7.5	1.912	18.6	65.52	0.64
50	48	337.6	54.9	29	5.1	5.604	10.6	36.67	0.35
50	48	194.6	43.6	35.8	8	1.843	12.6	48.15	0.47
50	48	343.6	32.3	31.9	3.7	35.68	7.6	19.51	0.19
50	48	233	58.8	30.8	4.8	1.457	9.6	27.08	0.2

[a] For linear regression analysis of nanocomplex fitness, the input parameters for the model included concentration (concn, nM), time of transfection (time, h), hydrodynamic size (diameter, nm; diameter error, nm), zeta potential (zeta, mV; zeta error, mV), valence of the tumor-penetrating ligand (LyP-1 valence), the overall charge of the peptide at neutral pH (peptide charge), percent of amino acids that is either lysine or arginine (%K and/or R), and the overall charge normalized by number of amino acids (charge density).

which may in turn affect the availability of siRNA inside the cytosol to bind to mRNA transcripts and participate in RNAi-mediated gene silencing.

Understanding Structure—Activity Relationships. Despite the consistency of the trends described above, the different fitness of nanocomplex candidates could only be partially explained by differences in cellular uptake, endosomal escape, and rate of nanocomplex dissociation. For example, the low fitness of PEN and VP22 peptides can be attributed to low cellular uptake and endosomal escape activity, which resulted in poor siRNA delivery into the cytosol that is available for RISC loading. In contrast, nanocomplexes such as 12R, 15R, and TP all showed high cellular uptake and endosomal escape activity; however, they differ significantly in fitness owing to differences in receptor-specificity. Therefore, other structural features of TP lacking in 12R or 15R may also dictate the efficiency and specificity

of siRNA transfection. As the optimized formulation likely resides within a much broader and more complex structural and functional space, a systematic screening of carrier structural parameters is needed to identify and understand key properties that could impact fitness.

To this end, we took a quantitative computational approach to systematically identify carrier properties that favored cell-type specific gene knockdown. We hypothesized that the relationship between carrier properties and fitness is likely to be linear; therefore, a linear regression approach that could establish a list of relative weights of significant model parameters was used.[31] Specifically, we chose a regression model to generate relationships between carrier fitness— the efficiency of cell type-specific gene knockdown taken at two different siRNA concentrations (100 nM and 50 nM) and at two time points (24 and 48 h post transfection)—and carrier structural properties,

including nanocomplex diameter, zeta potential, valence of the tumor-penetrating ligand LyP-1, peptide charge at physiologic pH, percent of lysines or arginines in the peptide sequence and charge density (Table 2). To generate the data for the model, we screened every combination of structural parameters to select ones that were linearly independent and individually significant (*t* test with $p < 0.05$). Measurements for each parameter were centered and scaled to ensure that the value of the associated regression coefficient is a direct measure of parameter importance. The parameter subset that resulted in a model that best matched the measured fitness for each individual nanocomplex was selected for further analysis ($R^2 = 0.74$, $F(1,29) = 13.9065$, $p < 10^{-6}$) (Figure 5A).

Two structural properties, namely the valence of the targeting ligand and the peptide charge, were found to be significant variables for explaining differences in nanocomplex fitness (Figure 5B). Namely, alterations in the valence of the targeting ligand or in peptide charge within the range of charges observed exert the largest influence on cell type-specific knockdown by the nanocomplex. Notably, the regression coefficient for peptide charge was the most negative, suggesting that lowering peptide charge might further enhance nanocomplex fitness. Consistent with our previous observations that multivalency favored high receptor-specificity, the regression coefficient for valence was the most positive, suggesting that increasing LyP-1 valence could also improve fitness.

To further validate the importance of LyP-1 valence and peptide charge in influencing cell type-specific gene knockdown, we separated all nanocomplex candidates into two groups based on their measured fitness values. Accordingly, nanocomplexes with high fitness (best fitness group) exhibited significantly higher peptide valence and lower peptide charge than those with low fitness as determined by one-way ANOVA ($F(1,34) = 19.5$, $p < 10^{-4}$ and $F(1,34) = 7.12$, $p < 0.01$, respectively), trends that were consistent with regression coefficients determined from the model (Figure 5C). Similar analysis for other selected parameters (concentration, diameter, zeta error, and charge density) did not yield statistically significant differences (data not shown). In aggregate, quantitative regression analysis enabled us to identify and validate two carrier structural properties—the valence of the targeting ligand and the peptide charge—that explained differences in nanocomplex fitness.

Quantifying the Multivalency Effect. Guided by the computational results, we further quantified the receptor-specificity and multivalency effects of the myr-TP-LyP-1 TPN. In four human cancer cell lines with varying p32 expression, we found that the uptake of TPN was enhanced relative to untargeted control nanocomplexes (UCN) bearing a scrambled peptide (TP-ARAL), and yet remained linearly correlated with surface p32 levels across different cell lines (Figure 6A and Supporting Information, Figure S4A,B). In contrast to LyP-1 peptides, TPN has a

Figure 5. Computational modeling to identify carrier structural properties that influence fitness. (A) Least square regression model used to predict carrier fitness *versus* measured fitness. The model is able to fit the data with $R^2 = 0.74$. Each data point represents the normalized fitness of a particular nanocomplex candidate at a specific siRNA concentration and time point post transfection. **(B)** Regression coefficients of the structural properties determined to be significant in predicting fitness. The nanocomplex valence of the targeting ligand and the peptide charge (black) have the highest impact on nanocomplex fitness. **(C)** Nanocomplex populations were separated into two groups based on individual fitness (best fitness and worst fitness). The average LyP-1 valence of the nanocomplex (left) and peptide charge (right) are calculated for each group and compared. Consistent with regression results, significant separations between the groups confirmed the positive impact of valence and the negative impact of peptide charge on fitness. (∗∗) $p < 0.01$; (∗∗∗∗) $p < 0.0001$.

higher affinity to cell surface p32, as demonstrated by the lower measured EC_{50} (concentration to produce 50% of maximal cellular binding) in two p32-expressing cell lines (Figure 6B and Supporting Information, Figure S4C). The apparent dissociation constant (K_D) of TPN was found to be 10−20 fold higher than that of LyP-1 ($K_{D,TPN} = 215$ nM; $K_{D,LyP-1} = 5.6\ \mu$M), consistent with multivalent nanoparticle systems reported elsewhere.[25] TPN uptake was saturated at higher concentrations, which further supports the interpretation that nanocomplexes were taken up in a receptor-mediated manner (Supporting Information, Figure S4D).

To better understand how the number of LyP-1 peptides displayed on the TPN influenced cellular binding, we synthesized nanocomplexes with a
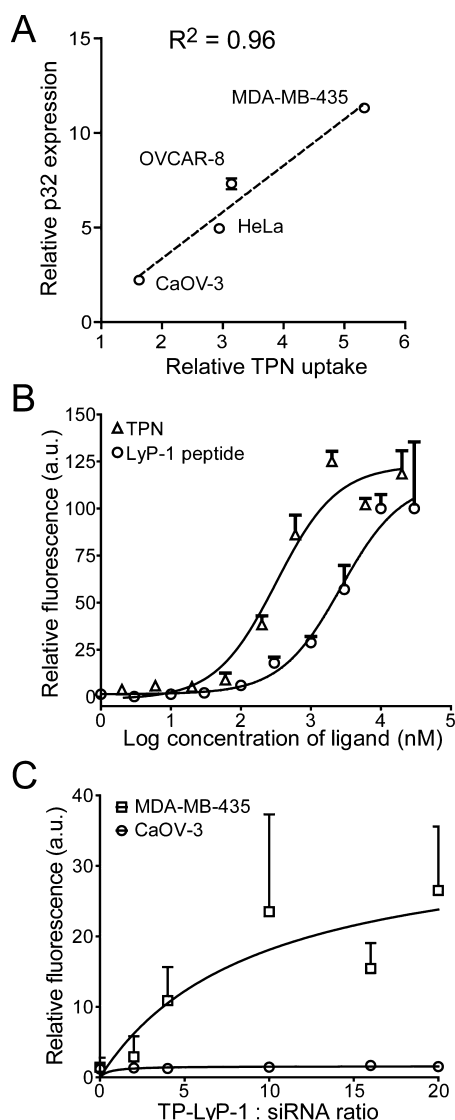
Figure 6. Multivalency effects of the myr-TP-LyP1 TPN. (A) The relationship between surface p32 levels and the cellular uptake of TPN carrying siRNA-VivoTag750 in cervical (HeLa), melanoma (MDA-MB-435) and ovarian (OVCAR-8 and Caov-3) cancer cells that express varying amounts of p32. Uptake was quantified using flow cytometry and normalized to that of a control nanocomplex (UCN). (B) Uptake of TPN *versus* monovalent LyP-1 peptide in MDA-MB-435 cells. Error bars indicate SD from three independent experiments. (C) Uptake of nanocomplexes bearing a mixture of TP-LyP-1 peptides and TP-ARAL peptides in MDA-MB-435 and Caov-3 cells measured by flow cytometry.

mixture of TP-LyP-1 and TP-ARAL peptides. Mixed nanocomplexes exhibited saturated uptake at a peptide-to-siRNA ratio of at least 10:1 (Figure 6C). As the density of LyP-1 ligands exceeds the amount of p32 available for binding, additional LyP-1 peptides will likely not engage in receptor-mediated endocytosis

and uptake will likely be saturated. Taken together, these results confirmed that p32 expression dictated siRNA delivery by multivalent nanocomplexes formed with myr-TP-LyP-1 tandem peptides.

CONCLUSIONS

To design vehicles for cell type-specific siRNA delivery, there are several barriers the delivery system must negotiate before achieving gene knockdown. These include receptor-mediated cellular binding, internalization by endocytosis, escape from endosomal sequestration into the cytosol, and ultimately, dissociation of siRNA from the carrier for RISC incorporation. Each step can influence the fate of the intracellular cargo, which in turn affects the receptor-specificity and efficiency of gene knockdown. Here, we have taken a systematic, quantitative approach to designing peptides and understanding their function in cell type-specific siRNA delivery. To this end, we synthesized a library of tandem peptides bearing a tumor-specific domain and distinct cell-penetrating domains, and formed nanocomplexes with siRNA through noncovalent interactions. A subset of nanocomplexes delivered siRNA to human cancer cell lines that express the cognate p32 receptor on the surface. We further evaluated the mechanism by which nanocomplexes delivered siRNA to the cytosol by characterizing cellular uptake, endosomal escape, and siRNA dissociation.

Comparative analysis of 18 tandem peptides revealed that variations in structural properties had a significant impact on receptor-specificity and gene silencing efficiency. Powered by linear regression modeling, we identified the valence of the targeting ligand on the nanocomplex and the overall peptide charge as key structural properties that favored cell-type specific gene silencing. The analysis led to the identification of the myristoylated tandem peptide, myr-TP-LyP-1, which condensed siRNA into multivalent nanocomplexes and effectively delivered siRNA in a cell-type specific manner. In comparison to systems that require localized activation of RNA interference, TPN-mediated siRNA delivery can seek out select cancer cells and deliver therapeutics to deep-seeded tumors.[32] Preclinical studies utilizing nanocomplexes to systemically deliver siRNA therapeutic to xenografts mouse models are currently underway. This advancement suggests that a systematic approach to the design of cell-penetrating peptides is essential for optimizing tumor-specific delivery of siRNA therapeutics for therapeutic applications.

METHODS

Cell Lines. HeLa and MDA-MB-435 cells were cultured in Dulbecco's modification of Eagle's medium (DMEM, purchased

from Invitrogen) with 10% bovine serum (Invitrogen), 5 IU penicillin, and 5 μg/mL streptomycin. OVCAR-8, OVCAR-4, and CaOV-3 cells were cultured in RPMI 1640 medium (Invitrogen) with 10% fetal bovine serum (FBS, Invitrogen), 2 mM glutamine,

5 IU penicillin, and 5 μg/mL streptomycin. All cells were cultured at 37 °C with 5% CO_2. OVCAR-4 and CaOV-3 cells were generously provided by Dr. William C. Hahn.

Peptides and siRNAs. The tandem peptides were synthesized *via* standard FMOC solid-phase peptide synthesis and purified by high-performance liquid chromatography at the MIT Biopolymers Core and Tufts University Core Facility. The peptides were then cyclized by bubbling air into 10 μM aqueous peptide solutions for 24 h, followed by lyophilization and storage at −20 °C. The effect of cyclization was confirmed by mass spectrometry. siRNAs were obtained from Dharmacon, Inc. The sequences of siRNAs (5′-3′) are: si*GFP* (GGCUACGUCCAGGAGCGCA).

Fluorescent Labeling of siRNA. siRNAs bearing 3′-amine on the sense strand was reacted with VivoTag S-750 amine-reactive dye (Visen Medical, Inc.) for 1 h at 37 °C. The reaction mixture was then precipitated overnight at −20 °C in 0.14 M NaCl and 70% ethanol, pelleted by centrifugation, washed, and air-dried. This labeling process was repeated to yield approximately 3.6 fluorophores per siRNA duplex.

DLS and Zeta Potential. Peptide-siRNA nanocomplexes were prepared by mixing siRNA in nuclease-free H_2O (20 μM) with each tandem peptide carrier (400 μM) at a molar ratio of 1:20 (siRNA:peptide) in $^1/_5$ of final volume in PBS for 10−15 min at room temperature. The hydrodynamic radii and zeta potential of nanocomplexes were determined using the zeta-potential and dynamic light scattering (DLS) instrument (Zetasizer-Nano, Malvern, Inc.).

Nanocomplex Library Gene Silencing and Uptake. HeLa cells expressing destabilized GFP were cultured in 96-well plates to *ca.* 70−80% confluence. siRNA (0−100 nM) was mixed with 20-fold molar excess of tetramethylrhodamine-labeled tandem peptides in PBS for 10−15 min at room temperature and added over cells for 4−6 h at 37 °C, after which the cells were washed extensively with PBS containing 10 U/mL heparin to remove unbound nanocomplexes and the medium was replaced. Transfection with Lipofectamine RNAiMAX was performed in accordance with the manufacturer's instructions. The cells were cultured for an additional 24−72 h before being examined by flow cytometry, analyzed by gating for propidium iodide-negative (live) cells.

To measure the cellular uptake of the TP-LyP1/siRNA nanocomplex, OVCAR-4, OVCAR-8, CaOV-3, and MDA-MB-435 cells were plated 48 h prior in 96-well plates and allowed to reach at least 70% in confluency. Nanocomplexes were added at 100 nM siRNA/2 uM peptide for 2 h at 37 °C in serum-free DMEM. Cells were then washed with PBS/heparin, trypsinized, and analyzed by flow cytometry (LSR II). For TP-LyP1 nanocomplex blocking experiments with anti-p32 antibody, OVCAR-8 cells were pre-incubated with anti-p32 polyclonal antibody at specified concentrations for 1 h at 37 °C before nanocomplex treatment.

Endosomal Escape. HeLa and OVCAR-8 cells were plated 48 h prior in 96-well plates and allowed to reach at least 70% in confluency. Calcein (0.25 mM) dye was added with or without various nanocomplex formulations (100nM siRNA) in complete medium (DMEM with 10% bovine serum) for 1 h at 37 °C. The cells were then washed three times with PBS and visualized live with a fluorescence microscope using the FITC filter. The number of cells with efficient endosomal escape as indicated by a diffuse cytoplasmic FITC fluorescence was counted from at least eight randomly selected fields of view and normalized to the total number of cells ($n = 500−800$ cells per carrier in each experiment).

Western Blotting. Cells were washed three times with 4 °C PBS, lysed in RIPA buffer (Millipore) containing protease inhibitor cocktail (Roche), subjected to electrophoresis on a 4−20% acrylamide gel (Bio-Rad), and transferred to a poly(vinylidenediluoride) membrane. The membrane was probed with anti-α-tubulin antibodies (Invitrogen) and polyclonal anti-p32 or anti-ID4 antibodies (Abcam) and detected with secondary antibodies (IRDye 680 goat antimouse IgG or IRDye 800 goat antirabbit IgG (Li-COR)). The blots were scanned using the Li-COR Odyssey infrared imaging system and the band intensities were quantified using Image J (http://rsbweb.nih.gov/ij/).

Inhibition of Endocytosis and Imaging. HeLa cells grown in 96-well plates at ∼70% confluence were incubated with small molecule inhibitors for 1 h at 37 °C, followed by incubation with nanocomplexes containing both labeled peptide (2 μM) and GFP siRNA (100 nM) for an additional hour at 37 °C. The cells were washed three times with cold PBS and were subsequently trypsinized for flow cytometry analysis. To visualize the intracellular trafficking of nanocomplexes along with endosomal markers, Lysotracker Red DND-99 (Invitrogen) or CellLight Early Endosomes-RFP (Invitrogen) was prior to the addition of nanocomplexes according to manufacturer's instructions.

Least Square Analysis. Least square analysis was performed using a custom built program in Matlab. To determine important structural parameters needed to predict fitness, we sequentially tested each combination of input parameters (nchoosek in matlab) and performed least-squares regression for each combination using the Matlab regstats function to fit the model and assess the significance of the fit (F statistic provided by regstats) and the significance of each individual parameter used in the model (T statistics provided by regstats). Parameter choices that led to F statistics with $p > 0.05$ or where any of the parameters had T statistic with $p > 0.05$ were not considered for further analysis. The program then checked that parameters do not suffer from damaging collinearity, which can result in uninformative regression weights.[31] To this end, we computed the variance inflation factor as $VIF = 1/(1 - R_i2)$, where R_i2 is the multiple correlation coefficient of parameter i regressed on the remaining parameters. VIF values above 10 are thought to be indicators of damaging collinearity. Parameter sets that suffered from collinearity were not considered for further analysis. Finally, of the parameter sets that yielded significant fits, using parameters that were individually significant to the model and did not suffer from damaging collinearity, we selected the model with highest R2, also measured using the regstats function.

Statistical Analysis. Statistical analyses were performed using built-in statistical functions in GraphPad Prism (GraphPad Software). Tumor burden between different cohorts and averaged fluorescence intensities from immunofluorescence staining, and Western blots were analyzed using one-way ANOVA and appropriate *posthoc* tests.

Conflict of Interest: The authors declare no competing financial interest.

Supporting Information Available: Characterization of tandem peptide, gene silencing by nanocomplexes, endosomal escape, and TP-LyP-1 delivery of siRNA is p32-dependent and multivalent. This material is available free of charge *via* the Internet at http://pubs.acs.org.

REFERENCES AND NOTES

1. Hopkins, A. L.; Groom, C. R. The Druggable Genome. *Nat. Rev. Drug. Discovery* **2002**, *1*, 727–730.
2. Pecot, C. V.; Calin, G. A.; Coleman, R. L.; Lopez-Berestein, G.; Sood, A. K. RNA Interference in the Clinic: Challenges and Future Directions. *Nat. Rev. Cancer.* **2011**, *11*, 59–67.
3. Whitehead, K. A.; Langer, R.; Anderson, D. G. Knocking Down Barriers: Advances in Sirna Delivery. *Nat. Rev. Drug Discovery* **2009**, *8*, 129–138.
4. Wolfrum, C.; Shi, S.; Jayaprakash, K. N.; Jayaraman, M.; Wang, G.; Pandey, R. K.; Rajeev, K. G.; Nakayama, T.; Charrise, K.; Ndungo, E. M.; *et al.* Mechanisms and Optimization of *in Vivo* Delivery of Lipophilic siRNAs. *Nat. Biotechnol.* **2007**, *25*, 1149–1157.
5. McNamara, J. O., 2nd; Andrechek, E. R.; Wang, Y.; Viles, K. D.; Rempel, R. E.; Gilboa, E.; Sullenger, B. A.; Giangrande, P. H.

Cell Type-Specific Delivery of siRNAs with Aptamer-siRNA Chimeras. *Nat. Biotechnol.* **2006**, *24*, 1005–1015.

6. Song, E.; Zhu, P.; Lee, S. K.; Chowdhury, D.; Kussman, S.; Dykxhoorn, D. M.; Feng, Y.; Palliser, D.; Weiner, D. B.; Shankar, P.; *et al.* Antibody Mediated *in Vivo* Delivery of Small Interfering RNAs *via* Cell-Surface Receptors. *Nat. Biotechnol.* **2005**, *23*, 709–717.

7. Akinc, A.; Zumbuehl, A.; Goldberg, M.; Leshchiner, E. S.; Busini, V.; Hossain, N.; Bacallado, S. A.; Nguyen, D. N.; Fuller, J.; Alvarez, R.; *et al.* A Combinatorial Library of Lipid-like Materials for Delivery of RNAi Therapeutics. *Nat. Biotechnol.* **2008**, *26*, 561–569.

8. van den Berg, A.; Dowdy, S. F. Protein Transduction Domain Delivery of Therapeutic Macromolecules. *Curr. Opin. Biotechnol.* **2011**, *22*, 888–893.

9. Gump, J. M.; June, R. K.; Dowdy, S. F. Revised Role of Glycosaminoglycans in TAT Protein Transduction Domain-Mediated Cellular Transduction. *J. Biol. Chem.* **2010**, *285*, 1500–1507.

10. Zorko, M.; Langel, U. Cell-Penetrating Peptides: Mechanism and Kinetics of Cargo Delivery. *Adv. Drug Delivery Rev.* **2005**, *57*, 529–545.

11. Tan, M.; Lan, K. H.; Yao, J.; Lu, C. H.; Sun, M.; Neal, C. L.; Lu, J.; Yu, D. Selective Inhibition of ERBB2-Overexpressing Breast Cancer *in Vivo* by a Novel Tat-Based ERBB2-Targeting Signal Transducers and Activators of Transcription 3-Blocking Peptide. *Cancer Res.* **2006**, *66*, 3764–3772.

12. Jiang, T.; Olson, E. S.; Nguyen, Q. T.; Roy, M.; Jennings, P. A.; Tsien, R. Y. Tumor Imaging by Means of Proteolytic Activation of Cell-Penetrating Peptides. *Proc. Natl. Acad. Sci. U.S.A.* **2004**, *101*, 17867–17872.

13. Vocero-Akbani, A. M.; Heyden, N. V.; Lissy, N. A.; Ratner, L.; Dowdy, S. F. Killing HIV-Infected Cells by Transduction with an HIV Protease-Activated Caspase-3 Protein. *Nat. Med.* **1999**, *5*, 29–33.

14. Sugahara, K. N.; Teesalu, T.; Karmali, P. P.; Kotamraju, V. R.; Agemy, L.; Girard, O. M.; Hanahan, D.; Mattrey, R. F.; Ruoslahti, E. Tissue-Penetrating Delivery of Compounds and Nanoparticles into Tumors. *Cancer Cell* **2009**, *16*, 510–520.

15. Sugahara, K. N.; Teesalu, T.; Karmali, P. P.; Kotamraju, V. R.; Agemy, L.; Greenwald, D. R.; Ruoslahti, E. Coadministration of a Tumor-Penetrating Peptide Enhances the Efficacy of Cancer Drugs. *Science* **2010**, *328*, 1031–1035.

16. Roth, L.; Agemy, L.; Kotamraju, V. R.; Braun, G.; Teesalu, T.; Sugahara, K. N.; Hamzah, J.; Ruoslahti, E. Transtumoral Targeting Enabled by a Novel Neuropilin-Binding Peptide. *Oncogene* **2011**, *31*, 3754–3763.

17. Ren, Y.; Cheung, H. W.; Von Maltzahn, G.; Agrawal, A.; Cowley, G. S.; Weir, B. A.; Boehm, J. S.; Tamayo, P.; Karst, A. M.; Liu, J. F.; *et al.* Targeted Tumor-Penetrating siRNA Nanocomplexes for Credentialing the Ovarian Cancer Target ID4. *Sci. Transl. Med.* **2012**, *4*, 147ra112.

18. Fogal, V.; Zhang, L.; Krajewski, S.; Ruoslahti, E. Mitochondrial/Cell-Surface Protein p32/gc1qR as a Molecular Target in Tumor Cells and Tumor Stroma. *Cancer Res.* **2008**, *68*, 7210–7218.

19. Laakkonen, P.; Porkka, K.; Hoffman, J. A.; Ruoslahti, E. A Tumor-Homing Peptide with a Targeting Specificity Related to Lymphatic Vessels. *Nat. Med.* **2002**, *8*, 751–755.

20. Pham, W.; Kircher, M. F.; Weissleder, R.; Tung, C. H. Enhancing Membrane Permeability by Fatty Acylation of Oligoarginine Peptides. *Chembiochem* **2004**, *5*, 1148–1151.

21. Frankel, A. D.; Pabo, C. O. Cellular Uptake of the TAT Protein from Human Immunodeficiency Virus. *Cell* **1988**, *55*, 1189–1193.

22. Elliott, G.; O'Hare, P. Intercellular Trafficking and Protein Delivery by a Herpesvirus Structural Protein. *Cell* **1997**, *88*, 223–233.

23. Derossi, D.; Joliot, A. H.; Chassaing, G.; Prochiantz, A. The Third Helix of the Antennapedia Homeodomain Translocates through Biological Membranes. *J. Biol. Chem.* **1994**, *269*, 10444–10450.

24. Pooga, M.; Hallbrink, M.; Zorko, M.; Langel, U. Cell Penetration by Transportan. *FASEB J.* **1998**, *12*, 67–77.

25. Montet, X.; Funovics, M.; Montet-Abou, K.; Weissleder, R.; Josephson, L. Multivalent Effects of RGD Peptides Obtained by Nanoparticle Display. *J. Med. Chem.* **2006**, *49*, 6087–6093.

26. Hong, S.; Leroueil, P. R.; Majoros, I. J.; Orr, B. G.; Baker, J. R., Jr.; Banaszak Holl, M. M. The Binding Avidity of a Nanoparticle-Based Multivalent Targeted Drug Delivery Platform. *Chem. Biol.* **2007**, *14*, 107–115.

27. Hu, Y.; Litwin, T.; Nagaraja, A. R.; Kwong, B.; Katz, J.; Watson, N.; Irvine, D. J. Cytosolic Delivery of Membrane-Impermeable Molecules in Dendritic Cells Using Ph-Responsive Core–Shell Nanoparticles. *Nano Lett.* **2007**, *7*, 3056–3064.

28. Sonawane, N. D.; Szoka, F. C., Jr.; Verkman, A. S. Chloride Accumulation and Swelling in Endosomes Enhances DNA Transfer by Polyamine–DNA Polyplexes. *J. Biol. Chem.* **2003**, *278*, 44826–44831.

29. Maurer-Stroh, S.; Eisenhaber, F. Myristoylation of Viral and Bacterial Proteins. *Trends Microbiol.* **2004**, *12*, 178–185.

30. McNaughton, B. R.; Cronican, J. J.; Thompson, D. B.; Liu, D. R. Mammalian Cell Penetration, siRNA Transfection, and DNA Transfection by Supercharged Proteins. *Proc. Natl. Acad. Sci. U.S.A.* **2009**, *106*, 6111–6116.

31. Belsley, D. A., *Regression Diagnostics: Identifying Influential Data and Sources of Collinearity*; Wiley-Interscience: Hoboken, N.J., 2004; p xv.

32. Shah, S.; Rangarajan, S.; Friedman, S. H. Light-Activated RNA Interference. *Angew. Chem., Int. Ed. Engl.* **2005**, *44*, 1328–1332.